

A Data-Driven Approach for Parameterizing Ocean Submesoscale Buoyancy Fluxes

Abigail Bodner¹, Dhruv Balwada², and Laure Zanna^{1,3}

¹Courant Institute of Mathematical Sciences, New York University, New York, NY, USA

²Lamont-Doherty Earth Observatory, Columbia University, Palisades, NY, USA

³Center for Data Science, New York University, New York, NY, USA

Key Points:

- A data-driven parameterization for mixed layer vertical buoyancy fluxes is developed using a Convolutional Neural Network (CNN).
- The CNN demonstrates high offline skill over a wide range of dynamical regimes and filter scales.
- We identify strong dependency on the large scale strain field, currently missing from oceanic submesoscale parameterizations.

arXiv:2312.06972v2 [physics.ao-ph] 3 Feb 2025

Abstract

Parameterizations of $O(1 - 10)$ km submesoscale flows in General Circulation Models (GCMs) represent the effects of unresolved vertical buoyancy fluxes in the ocean mixed layer. These submesoscale flows interact non-linearly with mesoscale and boundary layer turbulence, and it is challenging to account for all the relevant processes in physics-based parameterizations. In this work, we present a data-driven approach for the submesoscale parameterization, that relies on a Convolutional Neural Network (CNN) trained to predict mixed layer vertical buoyancy fluxes as a function of relevant large-scale variables. The data used for training is given from 12 regions sampled from the global high-resolution MITgcm-LLC4320 simulation. When compared with the baseline of a submesoscale physics-based parameterization, the CNN demonstrates high offline skill across all regions, seasons, and filter scales tested in this study. During seasons when submesoscales are most active, which generally corresponds to winter and spring months, we find that the CNN prediction skill tends to be lower than in summer months. The CNN exhibits strong dependency on the mixed layer depth and on the large scale strain field, a variable closely related to frontogenesis, which is currently missing from the submesoscale parameterizations in GCMs.

Plain Language Summary

Upper ocean turbulence is an important control on energy and heat exchanges between the atmosphere and ocean systems, and usually manifests at spatial scales that are too small to be resolved in climate models. Parameterizations are often used to estimate missing physics using information from the resolved flow. In contrast to traditional approaches, this work uses machine learning to predict unresolved properties of upper ocean turbulence. This new approach demonstrates high performance over a range of scales, locations and seasons, with potential to help reduce climate model biases.

1 Introduction

General Circulation Models (GCMs) and future climate change projections are notoriously sensitive to parameterizations of unresolved phenomena at the ocean-atmosphere interface (IPCC, 2019, 2021). Of particular importance is the ocean mixed layer, where turbulence modulates the transfer of properties – such as heat, momentum, and carbon – between the atmosphere and ocean interior (e.g., Frankignoul & Hasselmann, 1977; Bopp et al., 2015; Su et al., 2020). Turbulence in the ocean mixed layer spans a wide range of scales, from the $O(100)$ km mesoscales, to $O(1-10)$ km submesoscales, to $O(1-100)$ m boundary layer turbulence, and all the way down to the molecular scales. A sensitive dynamical interplay between turbulence across all relevant scales sets the stratification in the upper ocean (Treguier et al., 2023). As opposed to mixing and homogenization dominated by boundary layer turbulence, submesoscale flows play a particularly important role in contributing to vertical transport in the ocean mixed layer primarily by shoaling, or restratifying, the mixed layer (Boccaletti et al., 2007; McWilliams, 2016; Taylor & Thompson, 2023).

The restratification effect is at leading order a result of instabilities formed along mixed layer fronts– composed of sharp density gradients and vertically oriented isopycnals (Fox-Kemper et al., 2008; Gula et al., 2022). One of the primary submesoscale instabilities, known as mixed layer instabilities, produces vertical buoyancy fluxes (VBF) by slumping the fronts and restratifying the mixed layer. The effect of submesoscale restratification cannot be resolved in many GCMs, and is currently parameterized by the Mixed Layer Eddy parameterization (hereafter MLE, Fox-Kemper et al., 2011). Recent advances in submesoscale parameterization development propose new relationships between MLE and large scale properties of the mesoscale field (e.g., J. Zhang et al., 2023) and boundary layer turbulence (e.g., Bodner et al., 2023), yet these new approaches still

struggle to capture the full range of complexity (Lapeyre et al., 2006; Mahadevan et al., 2010; Bachman et al., 2017; Callies & Ferrari, 2018; Ajayi et al., 2021).

Data-driven methods are emerging as powerful tools, with the ability to capture highly complex relationships between variables in turbulent flows. Advances in machine learning based parameterizations have yielded promising results for subgrid closures such as for ocean mesoscale momentum fluxes (Bolton & Zanna, 2019; Zanna & Bolton, 2020; Guillaumin & Zanna, 2021; Perezhogin et al., 2023), ocean boundary layer mixing (Souza et al., 2020; Sane et al., 2023), and atmospheric boundary layer mixing (e.g., Yuval & O’Gorman, 2020; Wang et al., 2022; Shamekh et al., 2023). Numerous examples for other machine learning applications exist both in the atmosphere and the ocean for inference of flow patterns and structures from data (e.g., Chattopadhyay et al., 2020; Dagon et al., 2022; Xiao et al., 2023; Zhu et al., 2023).

Here, we introduce a data-driven approach for parameterizing submesoscale-induced VBF in the ocean mixed layer. We train a Convolutional Neural Network (CNN) using high-resolution simulation data, with the goal of learning an improved functional relationship between mixed layer VBF and the large-scale variables that help set it. The data used to train and test the CNN is sampled from the MITgcm-LLC4320 ocean model (hereafter LLC4320, Menemenlis et al., 2021), which simulated the global ocean at a resolution of $1/48^\circ$. The LLC4320 output has been widely studied for submesoscale applications, which cumulatively have demonstrated that submesoscale energetics and dynamics are captured relatively well down to its effective resolution (e.g., Rocha et al., 2016; Su et al., 2018; Gallmeier et al., 2023). In this paper, we describe the processing of the LLC4320 data and CNN architecture in section 2. Results and sensitivity tests of the CNN prediction on unseen data are presented and compared with the baseline of the MLE parameterization in section 3. In section 4, we apply two complimentary methods to explain the relationship learned by the CNN and the mixed layer VBF. Discussion and concluding remarks are given in section 5.

2 Data and methods

2.1 Processing the LLC4320

The LLC4320 is a $1/48^\circ$ Massachusetts Institute of Technology general circulation model (MITgcm), named after its Latitude-Longitude polar Cap (LLC) grid with 4320 points on each of the 13 tiles. The LLC4320 is initialized from the Estimating the Circulation and Climate of the Ocean (ECCO), Phase II project, and is forced at the surface by atmospheric reanalysis, at 6 hourly temporal resolution. Model output from a total of 14 months is available at hourly frequency from September 2011 to November 2012 (Forget et al., 2015; Menemenlis et al., 2008, 2021). Before computing the CNN input and output variables, a common processing procedure was applied to the LLC4320 data, as described below.

Since the primary goal of our work is to parameterize the impact of submesoscale processes on mixed layer stratification, we focus on diagnosing subgrid VBF (Fox-Kemper et al., 2008). The large-scale fields, which may be resolved in a coarse-simulation, and subgrid impacts, which need to be parameterized, are defined with the help of filters. This is similar to approaches commonly used in the large-eddy simulation literature (Sagaut, 2005). First, to reduce the data volume, we averaged all LLC4320 variables over periods of 12 hours, effectively time-filtering the fastest motions. Primarily composed of tides and internal waves, these fast-varying motions have minimal impact on the VBF and so the filtering operation does not account them (Balwada et al., 2018; Uchida et al., 2019). Next, a top-hat or coarsening spatial filter (denoted by $\bar{\cdot}$) was applied to decompose the simulation variables into large-scale and subgrid components. This allows us to de-

fine the subgrid VBF ($\overline{F^V}$) as:

$$\overline{F^V} = \overline{wb} - \overline{w}\overline{b}, \quad (1)$$

where \overline{w} and \overline{b} correspond to the large-scale variables that can be resolved on a coarse-grid, and \overline{wb} is the coarsened flux that is resolved in a high-resolution simulation. We used filter scales of $1^\circ, 1/2^\circ, 1/4^\circ, 1/8^\circ, 1/12^\circ$, which are defined by the width of the coarsening box, applied by averaging over a fixed number of grid points in the original LLC4320 grid. As an example for the $1/4^\circ$ spatial filter, averages are taken over 12×12 grid points of the $1/48^\circ$ simulation grid.

For simplicity, we restrict our approach to depth-averaged mixed layer properties, and to this end, all 3D variables are averaged over the mixed layer depth (denoted by superscript z hereafter). This also remains close to the formulation of the MLE parameterization (Fox-Kemper et al., 2011), where the parameterization is composed of a depth-independent amplitude and a vertical structure function that determines the shape of the parameterization over the mixed layer (Eq. (S3) in the supplementary material). Here, the mixed layer depth, H_{ML} , is defined as the depth at which the potential density anomaly, σ_0 , increased by 0.03 kg m^{-3} from its value at 10m depth (de Boyer Montégut et al., 2004). σ_0 is computed from the LLC4320 outputs of potential temperature and salinity fields, with reference pressure of 0 dbar and $\rho_0 = 1000 \text{ kg m}^{-3}$.

To ensure that the training data represented a diverse set of dynamics, we included a mix of regions with strong and weak variability (e.g., Torres et al., 2018) as shown by blue boxes in Fig. 1 (exact coordinates provided in Tab. S1). In the following section we describe how the LLC4320 data is processed for each of these regions to diagnose the vertical buoyancy flux (CNN output) and a variety of inputs (Tab. 1) in preparation for the CNN training.

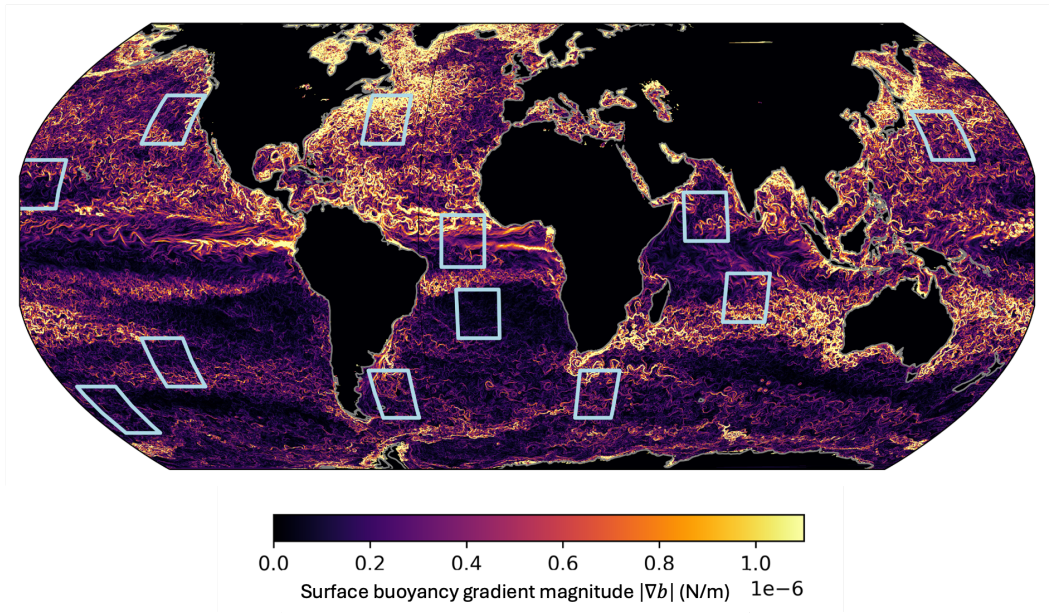


Figure 1. Snapshot of surface horizontal buoyancy gradient magnitude $|\nabla b|$ (N/m) given by the global LLC4320 simulation coarsened to $1/4^\circ$. Buoyancy gradients are a key contributor to the characteristics of submesoscale flows, and their properties vary significantly between regions and season (Fig. 2), motivating the choice of sampled regions used in this study (light blue boxes, exact coordinates listed in Tab. S1).

2.2 Input and output features

The subgrid quantity we are parameterizing using the CNN is the depth-averaged mixed layer VBF ($\overline{FV^z}$). This quantity is formally denoted as,

$$\mathbb{Y}_{wb} := \overline{FV^z} = \overline{w^z b^z} - \overline{w}^z \overline{b}^z. \quad (2)$$

VBF in the mixed layer is largely a result of submesoscale flows (Boccaletti et al., 2007). This can be seen in the maximum cross-spectrum of w and b , analogous to maximum VBF, which is found to be predominantly in the submesoscale range and confined to the mixed layer (Fig. 2a). However, variability across scales can defer between the different regions, and the filter scale choice (illustrated by the grey lines in Fig. 2b) will impact the properties of the large scale CNN inputs and subgrid flux output. We have included all regions to gain a variety of dynamical regimes in our training data, but test the performance of the CNN over the different filter scales, and selected unseen regions and parts of the timeseries in section 3.

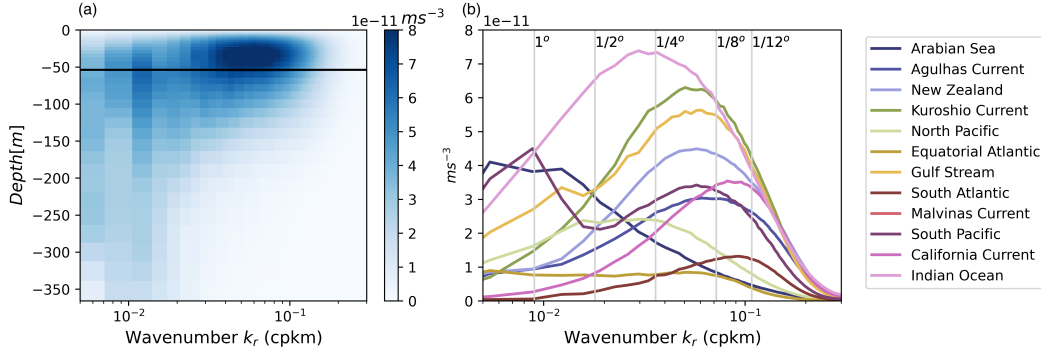


Figure 2. Isotropic cross-spectrum of w and b in variance-preserving form, averaged over the entire LLC4230 simulation duration (14 months): (a) Example of the depth varying cross-spectrum in the Gulf Stream region, illustrating that the VBF is concentrated in the small scales and within the average mixed layer (black horizontal line). (b) Cross-spectrum averaged over the mixed layer depth for all regions. Vertical gray lines mark the filter scales used in this study with respect to the cross-spectrum variability.

We choose to include input features that are correlated (Fig. S4), or have known analytical relationships, with submesoscale VBF. We leverage the physical relevance demonstrated by variables that appear in the MLE parameterization (Fox-Kemper et al., 2011; Bodner et al., 2023), as well as correlated large-scale velocity derivatives (e.g., Barkan et al., 2019; Balwada et al., 2021; J. Zhang et al., 2023). The input features (Tab. 1) consist of the depth-averaged horizontal buoyancy gradient magnitude, $|\overline{\nabla b^z}|$, where buoyancy is defined as $b = -g\sigma_0/\rho_0$, and $g = 9.81 \text{ m/s}^2$ is the gravity acceleration; Coriolis parameter, \overline{f} ; mixed layer depth, $\overline{H_{ML}}$; surface heat flux, \overline{Q} ; surface wind stress magnitude, $|\overline{\tau}| = \sqrt{\overline{\tau_x^2} + \overline{\tau_y^2}}$; boundary layer depth, $\overline{H_{BL}}$, an output of the LLC4320 computed from the Richardson number criteria with the critical value of 0.3 (K-profile Parameterization, Large et al., 1994); depth-averaged strain magnitude, $\overline{\sigma^z} = \sqrt{(\overline{u_x^z} - \overline{v_y^z})^2 + (\overline{v_x^z} + \overline{u_y^z})^2}$; depth-averaged vertical vorticity, $\overline{\zeta^z} = \overline{v_x^z} - \overline{u_y^z}$; depth-averaged horizontal divergence, $\overline{\delta^z} = \overline{u_x^z} + \overline{v_y^z}$. Note that velocities (u, v, w) and wind stresses (τ_x, τ_y) are all interpolated to collocate with the tracer grid.

Formally, we define our 9 input features as,

$$\mathbb{X} := (|\overline{\nabla b^z}|, \overline{f}, \overline{H_{ML}}, \overline{Q}, |\overline{\tau}|, \overline{H_{BL}}, \overline{\sigma^z}, \overline{\zeta^z}, \overline{\delta^z}), \quad (3)$$

and a single output as,

$$\mathbb{Y}_{wb} := \overline{w^z b^z} - \overline{wb^z} \quad (4)$$

The CNN provides a prediction of the subgrid fluxes as a function of the large scale variables, such that $S(\mathbb{X}) = \hat{\mathbb{Y}}_{wb}$ and $\hat{\mathbb{Y}}_{wb} \rightarrow \mathbb{Y}_{wb}$, where S represents the CNN and $\hat{\mathbb{Y}}_{wb}$ its prediction. Fig. 3 illustrates a schematic of the CNN with 9 input features and one output.

CNN inputs, \mathbb{X}

Depth-averaged buoyancy gradient magnitude	$ \overline{\nabla b^z} = \sqrt{(\overline{b_x^z})^2 + (\overline{b_y^z})^2}$
Coriolis parameter	\overline{f}
Mixed layer depth	$\overline{H_{ML}}$
Surface heat flux	\overline{Q}
Surface wind stress magnitude	$ \overline{\tau} = \sqrt{\overline{\tau_x^2} + \overline{\tau_y^2}}$
Boundary layer depth	$\overline{H_{BL}}$
Depth-averaged strain magnitude	$\overline{\sigma^z} = \sqrt{(\overline{u_x^z} - \overline{v_y^z})^2 + (\overline{v_x^z} + \overline{u_y^z})^2}$
Depth-averaged vertical vorticity	$\overline{\zeta^z} = \overline{v_x^z} - \overline{u_y^z}$
Depth-averaged horizontal divergence	$\overline{\delta^z} = \overline{u_x^z} + \overline{v_y^z}$

CNN Output, \mathbb{Y}_{wb}

Depth-averaged subgrid vertical buoyancy flux	$\mathbb{Y}_{wb} := \overline{w^z b^z} - \overline{wb^z}$
---	---

Table 1. Input (\mathbb{X}) and output (\mathbb{Y}_{wb}) features used in the CNN method. Overbar represents the top-hat spatial filter and superscript z represents a depth averaging over the mixed layer depth applied as part of the processing of the LLC4320 data (described in 2.2).

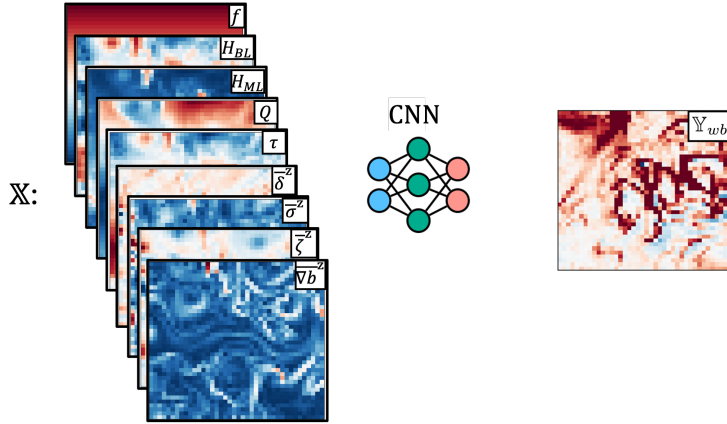


Figure 3. Schematic of the $1/4^\circ$ CNN method with 9 input features, \mathbb{X} , and one output, \mathbb{Y}_{wb} (corresponding to Tab. 1). The CNN architecture is described in section 2.3.

2.3 CNN architecture and training

Each experiment, designed with a given filter scale, is trained and tested independently, but all CNNs shared a common architecture. We use a CNN architecture for regression inspired by applications for mesoscale eddy parameterizations (Bolton & Zanna, 2019; Guillaumin & Zanna, 2021; Perezhugin et al., 2023). A hyper-parameter sweep over

the number of hidden layers, kernel size, learning rate, and weight decay, was used to find the best performing CNN. The CNN is trained over 100 epochs while minimizing the Mean Squared Error (MSE) loss (shown in Fig. S1). The hyperparameters were tuned against the $1/4^\circ$ filter scale experiment, and remained fixed throughout all other experiments. Results presented here are based on a CNN with a kernel size of 5×5 in the first layer, followed by 7 hidden convolutional layers with kernel size of 3×3 , a learning rate of 2×10^{-4} , and weight decay of 0.02. The total number of learnable parameters is approximately 300,000.

Prior to applying the CNN, all variables listed in Tab. 1 are normalized by a single mean and standard deviation computed over all regions (example shown in Fig. S2). To train the CNN, we randomly select 80% of the $\sim 10,000$ samples given from all regions combined. The remaining 20% is left unseen by the CNN, and is used to test the CNN prediction. Results are compared in the following section with the target LLC4320 data and the Bodner et al. (2023) version of the MLE parameterization, which is used here as a baseline. In subsections 3.1 and 3.2, we examine other split choices between the train and test datasets to include subsets of the sampled regions or timeseries, respectively.

3 CNN prediction of subgrid submesoscale fluxes

Once trained, the CNN has learned a functional mapping, $S(\mathbb{X})$, between the input features, \mathbb{X} , and subgrid mixed layer VBF, \mathbb{Y}_{wb} . In this section, we examine the extent to which the CNN can make skillful predictions on data that was not included in the training process. For this purpose, we compare the CNN prediction with the target LLC4320 data held out from training, and test whether the CNN improves on the baseline given by the Bodner et al. (2023) version of the MLE parameterization.

Illustrated by an example from the $1/4^\circ$ filter scale experiment (Fig. 4), the CNN is able to capture much of the fine-scale structure and sign of the subgrid VBF. The majority of the fluxes are positive, which is the bulk restratification effect inferred by the MLE parameterization. The negative fluxes exhibited in the LLC4320, and captured by the CNN but not the MLE parameterization, may be indicative of frontogenesis, where an ageostrophic secondary circulation intensifies the front (e.g., Hoskins & Bretherton, 1972; Shakespeare & Taylor, 2013). This can be further seen in the joint histogram of the VBF given by the target LLC4320 and those predicted by the CNN and MLE parameterizations (Fig. 5). The joint histograms are computed over the entire unseen test dataset, which provides a comparison over several orders of magnitude of the VBF. In the case of positive fluxes, the CNN prediction remains close to the LLC4320 VBF, as can be seen by the alignment along the one-to-one gray line, an improvement on the MLE parameterization which deviates from the LLC4320 VBF. For the negative fluxes, the one-to-one alignment is less pronounced, likely due to the significantly smaller number of negative samples seen by the CNN (less than 5% of the total samples). However, the ability of the CNN to predict of negative fluxes is still an improvement on the MLE parameterization, which does not include negative fluxes by construction.

To test whether the CNN also has skill in predicting bulk effects, such as is inferred by the MLE parameterization, the CNN predictions on unseen test data are averaged over each month to form a seasonal cycle, and is compared with the equivalent for the MLE parameterization and LLC4320 target data. We find that in all regions, the CNN prediction captures the seasonality and bulk effects of the LLC4320 data, and outperforms the MLE parameterization, particularly where fluxes appear to be strongest during the winter and spring months where the LLC4320 VBF can be as large as three times the MLE prediction (Fig. 6 for the $1/4^\circ$ filter scale experiment and more quantitatively in the analysis described below).

Prediction skill of the CNN and MLE parameterization for all filter scales are quantified in terms of R^2 values relative to the LLC4320 target data (calculation described in more detail in Eq. (S1)). We find that the CNN R^2 remain at a value of at least 0.2 higher than that of the MLE in all filter scale experiments and in all regions (Fig. 7). As the magnitude of Υ_{wb} varies spatially (Fig. 2), this impacts the predicted output of the CNN in the different regions. The largest filter scales tend to have skill nearing an R^2 values of 1, which then decreases as the filter scale becomes smaller. In the large filter scale experiments, the fields tend to be smoother, as much of the subgrid spatial variability is averaged out, thus presenting an easier learning problem for the CNN. The CNN prediction skill is found to be especially sensitive in the small filter scale experiments, where it performs well in some regions, e.g. in the California Current where all R^2 values are above 0.8, but less so in others, e.g. in the Indian Ocean region where the R^2 values in the small filter scale experiments are below 0.3). In the regions that exhibit large sensitivity to the filter scale such as the Kuroshio Current, Indian Ocean, and South Pacific, the skill of the MLE parameterization drops significantly as well.

It is worth noting that the CNN prediction skill can be sensitive to the initialization weights even when training identical experiment configurations (e.g., Otness et al., 2023). However, we find that for each given filter scale experiment, the sensitivity to the initialization weights is smaller than an R^2 value of 0.1 (Fig. S5), indicating that the large range of R^2 values displayed in Fig. 9 reflects the sensitivity due to regional variability rather than properties of the CNN.

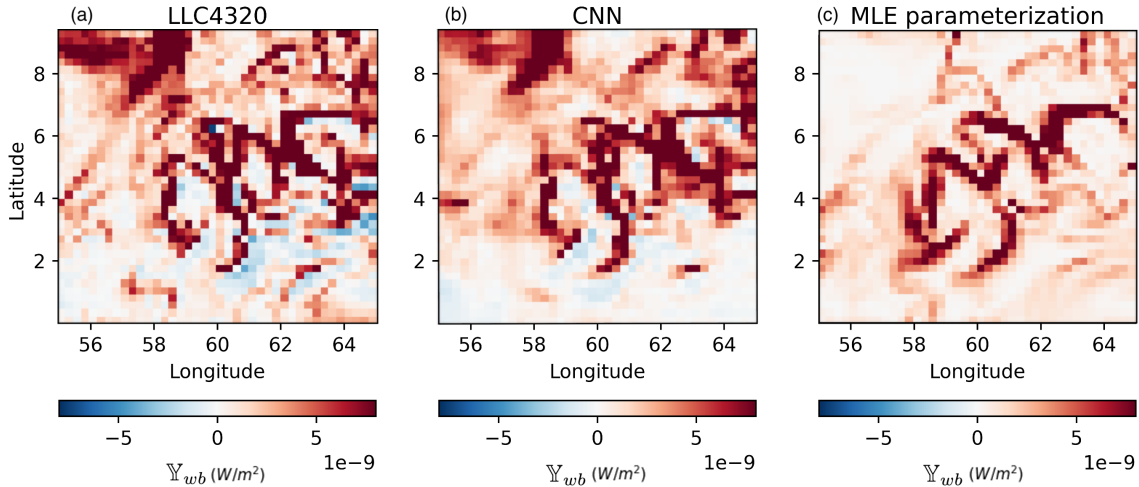


Figure 4. Snapshot taken from the Arabian Sea region of the depth-averaged subgrid VBF Υ_{wb} [W/m^2] given by (a) the LLC4320, (b) CNN prediction in physical space, and (c) the Bodner et al. (2023) version of the MLE parameterization. A $1/4^\circ$ filter scale is applied here. An example of (a) with filter scales of $1/12^\circ$, $1/8^\circ$, $1/2^\circ$, 1° is shown in Fig. S3.

As submesoscale seasonality greatly impacts the variability of VBF (demonstrated in Fig. 6), we examine the skill (in terms of R^2 values) of the CNN and MLE parameterization averaged only over winter and summer months (Fig. 8). During winter, when mixed layer VBF tend to be stronger, the skill of both the CNN and MLE parameterization in the smaller filter scale experiments drops compared with its equivalent in summer. This is particularly true for regions where fluxes are very strong during winter, such as in the Kuroshio Current, where the $1/8^\circ$ and $1/12^\circ$ filter scale experiments shows no skill (negative R^2) during winter compared with an R^2 value above 0.8 in summer. Sim-

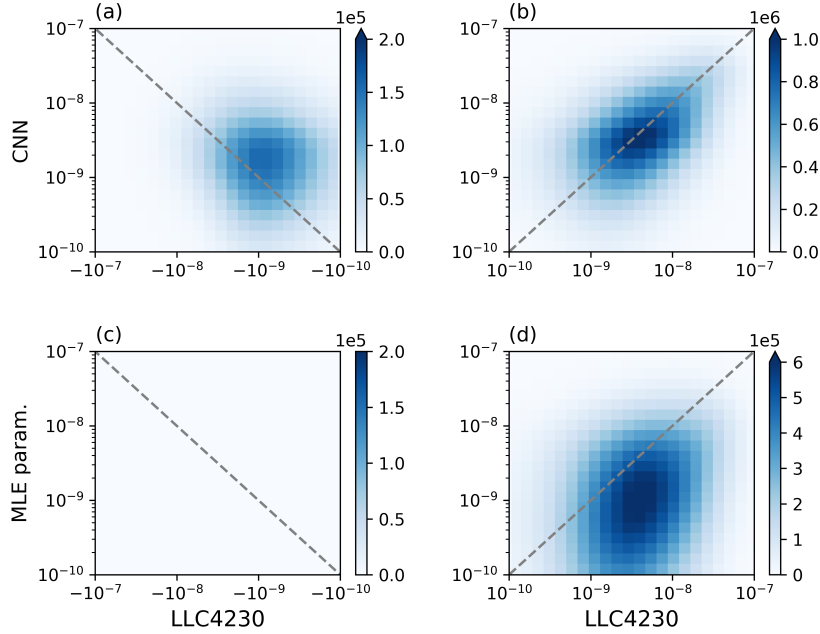


Figure 5. Joint histogram of the $1/4^\circ \mathbb{Y}_{wb}$ (W/m^2): (a,b) CNN prediction and LLC4230 data, and (c,d) MLE parameterization and LLC4230 data. Panels (a, c) correspond to negative fluxes and (b, d) to positive fluxes. The CNN predictions remain close to the target LLC4230 in both positive and negative values of \mathbb{Y}_{wb} . Note that the colorbar in (a) is an order of magnitude larger than the others due to the high concentration along the diagonal.

ilarly, the Gulf Stream, Agulhas Current, Malvinas Current, and the Southern Ocean near New Zealand all exhibit a drop in skill in both the MLE and CNN with small filter scales. In other regions with less of a pronounced seasonal cycle, such as in the South Pacific or South Atlantic regions, where the CNN skill is roughly the same for summer and winter, and differences appear within the 0.1 range that can be explained by the CNN initialization sensitivity. Interestingly, the R^2 values of the MLE parameterization still drops in both regions during winter in all filter scale experiments. These results suggest that both the CNN and the MLE parameterization struggle to predict the strongest fluxes, generally exhibited during winter and spring months (e.g., Callies et al., 2015; Johnson et al., 2016).

To better understand the dependency of our method on the training data, and in particular on regional and seasonal variability, in the following subsections we perform two sensitivity tests by holding out parts of the training data, retraining the CNN, and examining CNN prediction skill on unseen regions or selected fractions of the timeseries.

3.1 Holding out regions from training

We test the ability of the CNN to make predictions on regions that are not included in the training data. We thus generate 12 new datasets that correspond to removing one region at a time from the training dataset. We retrain the CNN in 12 different experiments, and make predictions on a different unseen region each time. The R^2 values of the CNN on the unseen regional data (Fig. 9) remain consistent with those found on the full training set (Fig. 7) across filter scales and over all regions. This suggests that the training data covers a wide enough range of dynamical regimes that enables generaliza-

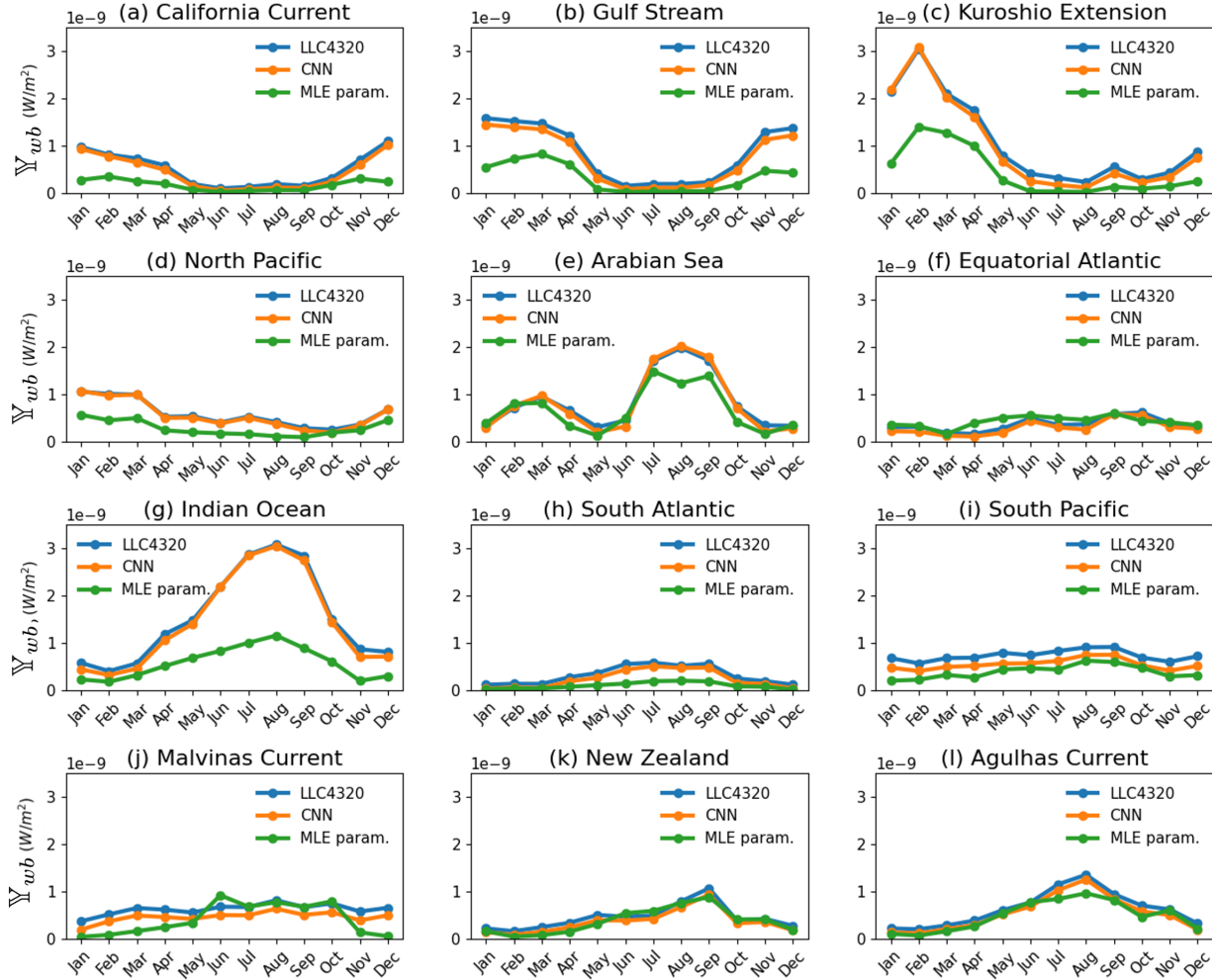


Figure 6. Area-weighted spatial average of \mathbb{Y}_{wb} (W/m^2) decomposed by region in the $1/4^\circ$ filter scale experiment. In each panel, CNN predictions of \mathbb{Y}_{wb} on unseen test data (orange) are averaged over each month and compared with the LLC4320 target data (blue) and the MLE parameterization (green). In all regions, the CNN prediction stays close to the LLC4320 target data and surpasses estimates from the MLE parameterization.

tion of the CNN on regions not included in training, an especially important result given that a fairly small number of regions were included in training compared with the full ocean.

3.2 Holding out seasonality from training

We perform two experiments in which we hold out winter and summer months from the training data, to examine the ability of the CNN to make predictions on unseen seasonal variability. We thus create two new training and test datasets to better understand the overall sensitivity of our method to submesoscale seasonality:

- **Winter held out** refers to training data which excludes from the time series the months of January, February, March from all regions in the Northern Hemisphere,

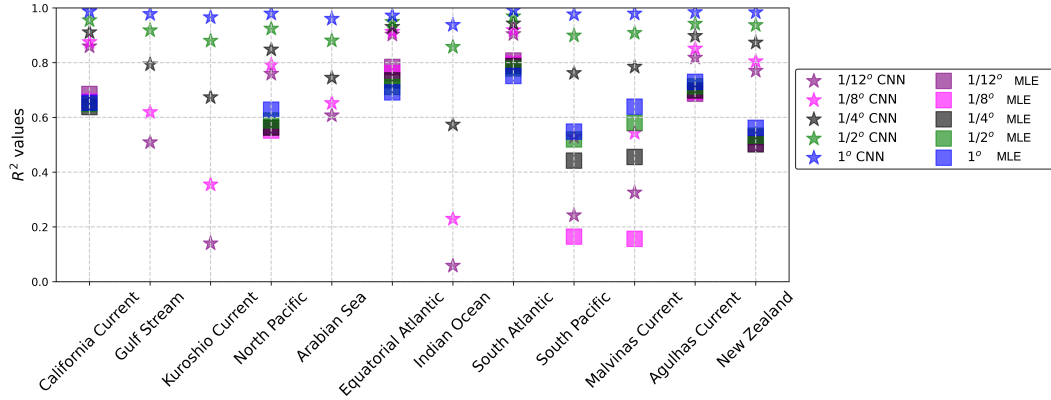


Figure 7. R^2 values of CNN prediction on unseen data (stars) and the MLE parameterization estimates (squares) decomposed by regions. Colors represent the different filter scale experiments. Note that R^2 is a point-wise estimate and not an averaged quantity as in Fig. 6. Negative R^2 values, exhibited in the South Pacific and Malvinas Current regions in the MLE parameterization, are removed from this figure. The CNN skill exceeds that of the MLE parameterization in all regions and for all filter scales.

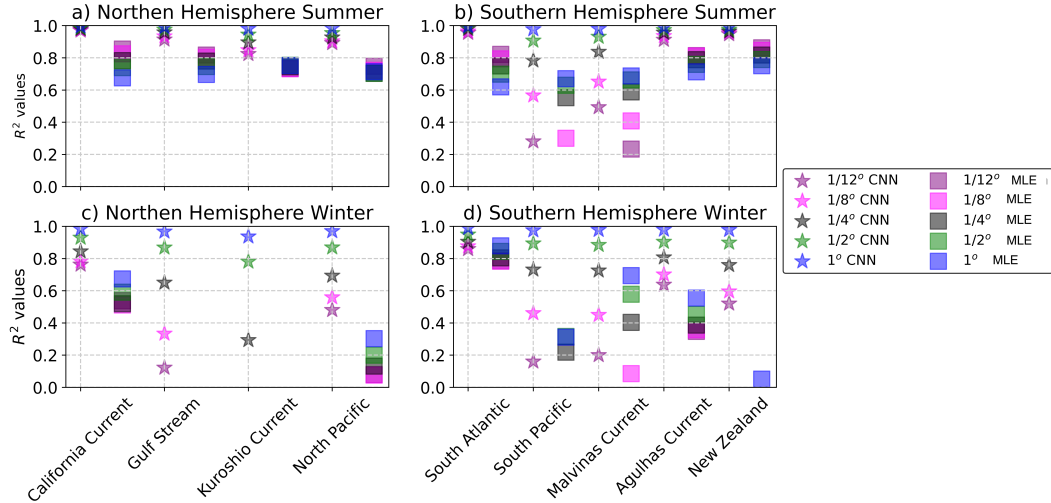


Figure 8. Same as Fig. 7, R^2 values of CNN prediction on unseen data (stars) and the MLE parameterization estimates (squares) decomposed by regions. Colors represent the different filter scale experiments. Here we include an average over winter (summer) months: January, February, March and summer (winter) months: July, August, September for regions in the Northern (Southern) Hemisphere. The CNN skill is generally higher in summer (week VBF) compared with winter (strong VBF). Note that we have not included equatorial regions here as the submesoscale equatorial seasonality is less trivial.

and July, August, September from regions in the Southern Hemisphere. Note again that we have removed equatorial regions from the analysis entirely. The remainder of the time series— e.g. spring, summer, fall— is used to train the CNN, and predictions are made on the unseen winter data.

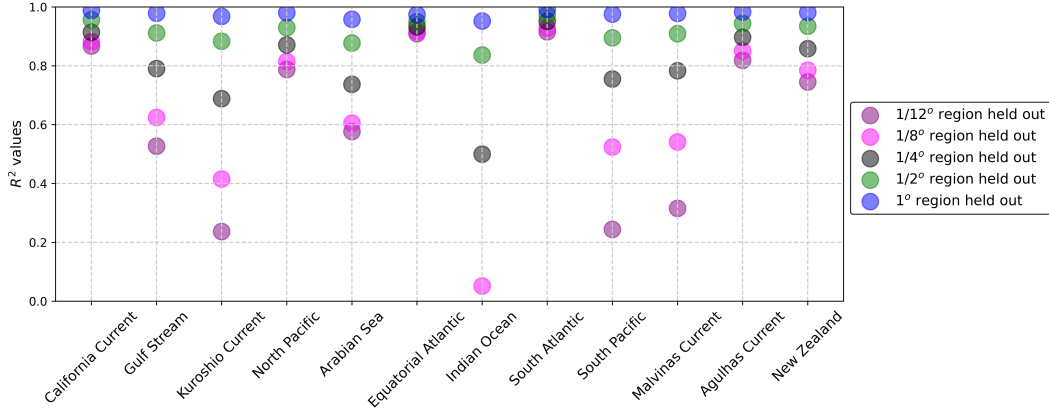


Figure 9. R^2 values of CNN prediction on regions held out during training. Colors represent the different filter scale experiments. Results are consistent with Fig. 9 which include all regions for training, suggesting that the CNN is able to generalize onto unseen regions.

- **Summer held out** is same as the above, where we now exclude July, August, September from the Northern Hemisphere and January, February, March from the Southern Hemisphere. Equatorial regions are once again excluded.

In these experiments, we find that results differ between regions in the Northern and Southern Hemispheres. In the Northern Hemisphere regions, the R^2 values in the "Summer held out" experiments decrease by a margin larger than 0.1 compared with the CNN trained on the full timeseries (Fig. 10a compared with Fig. 8). We find the largest decreases in particular in the small filter scale experiments in regions affected by strong ocean boundary currents (i.e., the Gulf Stream and Kuroshio Current). Contrarily, the Southern Hemisphere regions are found to be consistent with the predictions for experiments trained on the full timeseries (Fig. 10b and Fig. 8). The CNN predictions in the "Winter held out" experiments result in lower R^2 values in the Northern Hemisphere (Fig. 10c) compared with predictions trained on the the full timeseries. In the Kuroshio Current for example, all filter scales smaller than 1° result in negative R^2 values, indicating that there is no skill in the CNN prediction in these cases. In the Southern Hemisphere regions (Fig. 10d), the "Winter held out" experiments also display a decrease in R^2 values but it is still within the margin that can be explained by sensitivity to the initialization weights (Fig. S5). These results reinforce the need for the distribution of the data used to train the CNN to include the strongest seasonal fluxes, and particularly from regions where submesoscales are most active, such as near ocean boundary currents.

Results from both the seasonal and regional sensitivity experiments indicate that the learned relationships between the input features and \mathbb{Y}_{wb} can extend over a variety of dynamical regimes, especially in the large filter scale experiments. In the following section we delve deeper in attempt to interpret these relationships.

4 Local and non-local feature importance

We have shown that the CNN improves on the MLE parameterization, but an important remaining question is why? What relationships are learned between the input variables and \mathbb{Y}_{wb} that lead to better predictions by the CNN? With such complex and nonlinear relationships, it is difficult to decipher which input feature is most important and for what reason. Many methods exist that help explain and interpret the dependency of CNN outputs to its inputs (e.g., Zeiler & Fergus, 2014; Ribeiro et al., 2016; Selvaraju

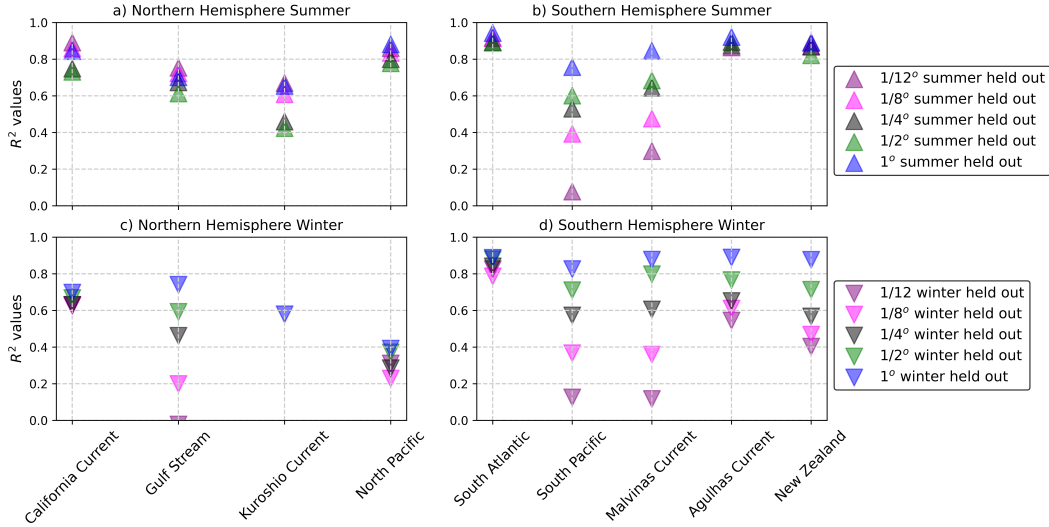


Figure 10. R^2 values of CNN prediction on seasons held out during training: summer (upward triangle), winter (downward triangle). Colors represent the different filter scale experiments. Same as Fig. 8, we average over winter (summer) months: January, February, March and summer (winter) months: July, August, September for regions in the Northern (Southern) Hemisphere. The CNN skill in the Northern Hemisphere regions, in particular near strong ocean boundary current, drops compared with its equivalent in Fig. 10.

et al., 2017; Van den Broeck et al., 2022). Here, we have chosen two complimentary methods that help gain insight on the learned relationships and the importance of individual inputs to \mathbb{Y}_{wb} .

4.1 Impact of input feature on CNN prediction skill

To test the dependency of the CNN prediction on certain input features, we perform a set of ablation experiments, where we remove one input feature at a time, retrain the CNN, and examine the resulting prediction skill in terms of the relative R^2 value. This relative R^2 value is taken as the difference between R_{all}^2 , resulting from the experiment with all input features included, and R_{abl}^2 , resulting from the ablation experiment for each input. A high $R_{all}^2 - R_{abl}^2$ value indicates that the skill has dropped in a particular ablation experiment, meaning that the CNN strongly depends on said input feature (top panels in Fig. 11). Notably, strain demonstrates the strongest dependency of the CNN consistently across all filter scales. Interestingly, there appears to be very little sensitivity to the removal of any other input feature, including those used by the MLE parameterization.

4.2 Sensitivity of output relative to input features

We next apply a complimentary method to the ablation experiment above. The Jacobian of the CNN prediction, $S(\mathbb{X})$, is computed with respect to the input features by taking gradients along the CNN weights, $\nabla_{\mathbb{X}} S(\mathbb{X})$. The Jacobian is an especially useful metric to evaluate the point-wise sensitivity of the output to each input feature (e.g., Ross et al., 2023). Note that unlike the ablation experiment, where we examined the R^2 value on the full output domain, the Jacobian considers only the sensitivity of a single output grid cell to a single grid cell in the input feature map. Here, we compute the Ja-

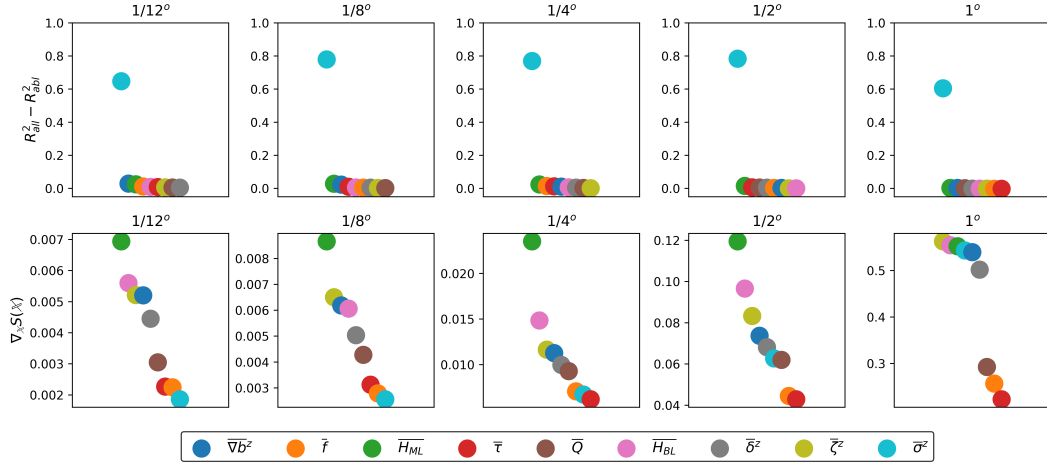


Figure 11. Explainability methods: Top panels are the relative R^2 values, $R^2_{all} - R^2_{abl}$, between the CNN containing all input features and results from the ablation experiment, where one input feature is removed at a time. Bottom panels are the Jacobian $\nabla_{\mathbb{X}}S(\mathbb{X})$ of the output with respect to individual inputs (in normalized units). In both methods, a high score indicates sensitivity to input features. Columns represent the filter scale experiments. Note that the entire unseen dataset (including all regions and seasons) was used here.

cobian over the entire unseen test dataset, and examine its *average* values for each input feature, thus providing a metric for how sensitive, on average, the CNN output is to each input feature. We contrast the Jacobian with the $R^2_{all} - R^2_{abl}$ values given by the ablation experiments (Fig. 11), where for the Jacobian, a high score indicates that the CNN prediction, $S(\mathbb{X})$, is sensitive to point-wise changes in a certain input. We find that the highest-ranked input feature, for which $S(\mathbb{X})$ is most sensitive to, is the mixed layer depth, H_{ML} , which is generally a one-dimensional, local property determined by surface forcing. The sensitivity to mixed layer depth is followed by sensitivity to boundary layer depth, the buoyancy gradient, and vorticity. Note that $S(\mathbb{X})$ does not appear to be sensitive to point-wise changes in surface heat flux, surface wind stress, or Coriolis, which is likely due to these fields being smoother in the LLC4320 at the scales relevant for the Jacobian. Despite strain being the most important feature in the previous section, it is only in the 1° filter scale experiment that the Jacobian exhibits sensitivity of $S(\mathbb{X})$ to vorticity, divergence, and strain, indicating that the impact of these fields is most apparent at the large scale.

4.3 Receptive field of the CNN

To further understand the relevance of locality, we follow the analysis in Ross et al. (2023) for examining the Jacobian of the output center point with respect to the full domain of each input feature. An example for the buoyancy gradient input feature is shown in Fig. 12a, where the shaded area illustrates the CNN’s receptive field needed to predict a single output point. Averaging over that halo, we examine the fraction of Jacobian over the number of grid points, which can be thought of as the percentage of sensitivity for each input feature that is being captured by the CNN (Fig. 12b,c). We find that 7 grid points away from the center is sufficient for capturing 90% of the Jacobian fraction, e.g. 90% of sensitivity between the output and input features. A relatively local receptive field is found to be consistent across filter scales despite the varying importance of input features found previously.

This result complements the analysis in Gultekin et al. (2024), which found that the Guillaumin and Zanna (2021) CNN skill saturates at a stencil of seven grid points for coarse-graining factors of 4, 8, 12, 16. As discussed in 2.3, the CNN architecture choice used here is motivated by that used in Guillaumin and Zanna (2021), however, the physical phenomena we are parameterizing is different, and so are the input and output features. An investigation of the significance of a seven grid point stencil and its dependence on the CNN architecture in both cases is left for a future study.

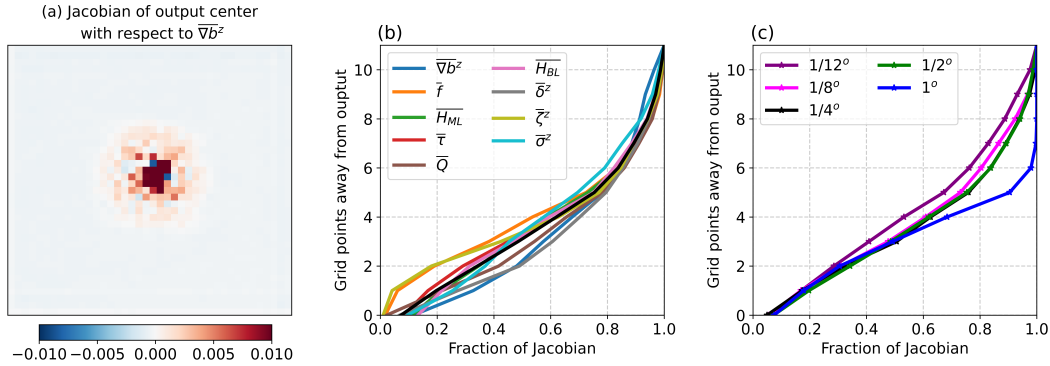


Figure 12. (a) Example of the Jacobian at the center of the input domain with respect to the buoyancy gradient field in a $1/4^\circ$ filter scale experiment. (b) Radial grid point number compared with fraction of $\nabla_{\mathbb{X}}S(\mathbb{X})$ for all input features in the $1/4^\circ$ filter scale experiment. Black line is the mean over all inputs. (c) Average fraction of Jacobian for all filter scales experiments. We find that 7 grid points captures 90% of the Jacobian fraction, which corresponds to the number of grid points required to capture sensitivity between the input map and a single output grid cell. In all panels the Jacobian is computed in normalized units.

5 Discussion and Conclusions

The parameterization for submesoscale VBF plays a key role in setting stratification in the ocean mixed layer, and as such contributes to the exchange between the ocean and atmosphere systems in GCMs. In contrast to previous physics-based approaches, here we develop a new data-driven parameterization, where a CNN is trained to predict mixed layer VBF. The subgrid flux, \mathbb{Y}_{wb} , is inferred by the CNN as a function of 9 large-scale input features with known relevance to submesoscale VBF: $\overline{\nabla b^z}$, f , H_{ML} , N^2 , Q , τ , H_{BL} , $\bar{\sigma}^z$, $\bar{\delta}^z$, $\bar{\zeta}^z$ (see Tab. 1). The data used for training is given from 12 regions sampled from the global high-resolution LLC4320 simulation output. The CNN is trained over a random selection of 80% of all data, while the remaining 20% is unseen by the CNN and is used for testing. We perform five filter scale experiments of $1/12^\circ$, $1/8^\circ$, $1/4^\circ$, $1/2^\circ$, 1° and compare with a baseline given by the Bodner et al. (2023) formulation of the MLE parameterization.

We consistently find that the CNN predictions improve on the MLE parameterization, with higher R^2 values across all regions, seasons, and filter scales tested in this study. We additionally perform several sensitivity experiments, where we test the CNN's ability to make predictions on regional or temporal data held out during training. It is found that the CNN, in particular in the larger filter scale experiments, is able to make skillful predictions on unseen data, but does poorly during when submesoscales are most active, generally corresponding to winter months and near ocean boundary currents.

The significant improvement on the MLE parameterization indicates that the CNN has learned new meaningful relationships between the input features and \mathbb{Y}_{wb} , such that it is able to make skillful predictions over widely different dynamical regimes. We applied two complimentary explainability methods which enable a closer look at the relationships between the CNN output and input features. We find that the CNN exhibits strong dependency on the local relationship between \mathbb{Y}_{wb} and the mixed layer depth, a 1D property driven by surface forcing, and strong non-local dependency on the large scale strain field, a variable closely related to frontogenesis, which is currently missing from the MLE parameterization in GCMs.

An important limitation of these method is in detecting the importance of features that are strongly correlated with other fields, such that removing one feature may not lead to differences in the CNN prediction skill. In particular, fields associated with surface forcing, e.g., mixed layer, boundary layer, surface heat flux, and wind stress are expected to be correlated (as is also found to be true in the LLC4320 data, Fig. S4). Nonetheless, results from the ablation experiments suggest that the primary reason the CNN predictions surpass those of the MLE parameterization are due to the newly-captured non-local relationship between \mathbb{Y}_{wb} and the large scale strain field, on which the CNN is strongly dependent. Note that strain is known for its role in constraining submesoscale fluxes and contributing to frontal intensification (e.g., Shcherbina et al., 2013; Balwada et al., 2021; Sinha et al., 2023), but these findings emphasize the relevance of strain to improving submesoscale VBF parameterizations, such as recently proposed by J. Zhang et al. (2023). An extension of these approaches may include incorporating more data from other submesoscale permitting simulations (Uchida et al., 2022; Gultekin et al., 2024), or an investigation of causal links which are not captures in the current framework (e.g., Camps-Valls et al., 2023). An equation discovery approach (e.g., Zanna & Bolton, 2020) may enable a closer comparison with J. Zhang et al. (2023), and whether the relationship between strain and submesoscale fluxes emerge in a similar fashion.

We have demonstrated that the CNN improves on the MLE parameterization in an offline setting. However, it is important to note that during training, the CNN minimizes the MSE loss— a metric closely related to the R^2 value (as shown in Eq. (S1)). The MLE parameterization, on the other hand, is designed to represent the bulk effects of submesoscale VBF. A next important step is to explore the implications of better captured mixed layer VBF in a GCM and compare with the MLE parameterization online, such as in a recent attempt by Zhou et al. (2024) in Regional Ocean Modeling System (ROMS). We have designed our method to correspond with the existing implementation of the MLE parameterization in GCMs, where the theoretical expression for \mathbb{Y}_{wb} in Eq. (S2) can simply be replaced with the CNN. A relatively small receptive field of 7 grid points is found to be sufficient at capturing relationships between the input features and \mathbb{Y}_{wb} , which suggests that a smaller network may aid future implementation efforts in GCMs (C. Zhang et al., 2023). A decomposition may be preferred to distinguish the bulk restratification effect with the intermittent negative fluxes, and will allow a more natural relationship with vertical buoyancy fluxes already estimated in boundary layer turbulence parameterizations (Large et al., 1994; Reichl & Hallberg, 2018; Sane et al., 2023). The exact formulation, implementation, and evaluation of impact on climate variables is left for future work.

Beyond the modeling framework discussed above, the utility of our work can also be made amenable to observational data. In particular, the Surface Water and Ocean Topography (SWOT) altimeter mission is starting to provide measurements of sea surface height at an unprecedented resolution (Morrow et al., 2019). The data-driven approach presented here provides an opportunity to leverage surface fields derived from SWOT (e.g., Qiu et al., 2016; Bolton & Zanna, 2019), to infer subsurface VBF and gain new insights of upper ocean dynamics.

Open data

Data from the LLC4320 simulation can be accessed using the `llcreader` Python package (Abernathy, 2019). Variables from the LLC4320 output in the regions used in this study are stored on the LEAP-Catalog <https://catalog.leap.columbia.edu/feedstock/highresolution-ocean-simulation-llc4320-12hourly-averaged-3d-regions>. Code used to process the LLC4320, train the CNN, and generate the figures in this manuscript can be found at https://github.com/abodner/submeso_param_net. Diagnostics incorporate open source Python packages: `xhistogram`, `xhistogram.readthedocs.io`; `fastjmd95`, (Abernathy, 2020) ; `xmitgcm`, (Abernathy et al., 2021).

Acknowledgements

This research received support through Schmidt Sciences, LLC. AB was supported by a grant from the Simons Foundation: award number 855143, Bodner. We thank members of the M²LInES project for support and constructive feedback during the formulation of ideas, in particular, Pavel Perezhogin, Chris Pedersen, Ryan Abernathy, Carlos Fernandez-Granda, and Fabrizio Falasca. The authors would also like to thank the Pangeo Project for providing open-source code which enabled timely analysis for working with the LLC4320 data. This research was also supported in part through the NYU IT High Performance Computing resources, services, and staff expertise.

References

- Abernathy, R. (2019). *Petabytes of ocean data, part i: Nasa ecco data portal*.
- Abernathy, R. (2020). fastjmd95: Numba implementation of jackett & mcdougall (1995) ocean equation of state. *Zenodo [code]*, 10.
- Abernathy, R., Busecke, J., Smith, T., Banihirwe, A., Fernandes, F., Bourbeau, J., ... others (2021). xgcm: General circulation model postprocessing with xarray. *Zenodo [code]*, 10.
- Ajayi, A., Le Sommer, J., Chassignet, E. P., Molines, J.-M., Xu, X., Albert, A., & Dewar, W. (2021). Diagnosing cross-scale kinetic energy exchanges from two submesoscale permitting ocean models. *Journal of Advances in Modeling Earth Systems*, 13(6), e2019MS001923.
- Bachman, S. D., Fox-Kemper, B., Taylor, J. R., & Thomas, L. N. (2017). Parameterization of frontal symmetric instabilities. i: Theory for resolved fronts. *Ocean Modelling*, 109, 72–95.
- Balwada, D., Smith, K. S., & Abernathy, R. (2018). Submesoscale vertical velocities enhance tracer subduction in an idealized antarctic circumpolar current. *Geophysical Research Letters*, 45(18), 9790–9802.
- Balwada, D., Xiao, Q., Smith, S., Abernathy, R., & Gray, A. R. (2021). Vertical fluxes conditioned on vorticity and strain reveal submesoscale ventilation. *Journal of Physical Oceanography*, 51(9), 2883–2901.
- Barkan, R., Molemaker, M. J., Srinivasan, K., McWilliams, J. C., & D’Asaro, E. A. (2019). The role of horizontal divergence in submesoscale frontogenesis. *Journal of Physical Oceanography*, 49(6), 1593–1618.
- Boccaletti, G., Ferrari, R., & Fox-Kemper, B. (2007). Mixed layer instabilities and restratification. *Journal of Physical Oceanography*, 37(9), 2228–2250.
- Bodner, A. S., Fox-Kemper, B., Johnson, L., Van Roekel, L. P., McWilliams, J. C., Sullivan, P. P., ... Dong, J. (2023). Modifying the mixed layer eddy parameterization to include frontogenesis arrest by boundary layer turbulence. *Journal of Physical Oceanography*, 53(1), 323–339.
- Bolton, T., & Zanna, L. (2019). Applications of deep learning to ocean data inference and subgrid parameterization. *Journal of Advances in Modeling Earth Systems*, 11(1), 376–399.
- Bopp, L., Lévy, M., Resplandy, L., & Sallée, J.-B. (2015). Pathways of anthropogenic carbon subduction in the global ocean. *Geophysical Research Letters*, 42(15), 6416–6423.
- Callies, J., & Ferrari, R. (2018). Baroclinic instability in the presence of convection. *Journal of Physical Oceanography*, 48(1), 45–60.
- Callies, J., Ferrari, R., Klymak, J. M., & Gula, J. (2015). Seasonality in submesoscale turbulence. *Nature communications*, 6(1), 6862.
- Camps-Valls, G., Gerhardus, A., Ninad, U., Varando, G., Martius, G., Balaguer-Ballester, E., ... Runge, J. (2023). Discovering causal relations and equations from data. *Physics Reports*, 1044, 1–68.
- Chattopadhyay, A., Hassanzadeh, P., & Pasha, S. (2020). Predicting clustered weather patterns: A test case for applications of convolutional neural networks to spatio-temporal climate data. *Scientific reports*, 10(1), 1317.
- Dagon, K., Truesdale, J., Biard, J. C., Kunkel, K. E., Meehl, G. A., & Molina, M. J. (2022). Machine learning-based detection of weather fronts and associated extreme precipitation in historical and future climates. *Journal of Geophysical Research: Atmospheres*, 127(21), e2022JD037038.
- de Boyer Montégut, C., Madec, G., Fischer, A. S., Lazar, A., & Iudicone, D. (2004). Mixed layer depth over the global ocean: An examination of profile data and a profile-based climatology. *Journal of Geophysical Research: Oceans*, 109(C12).
- Forget, G., Campin, J.-M., Heimbach, P., Hill, C., Ponte, R., & Wunsch, C. (2015). Ecco version 4: An integrated framework for non-linear inverse modeling and

- global ocean state estimation. *Geoscientific Model Development*, 8(10), 3071–3104.
- Fox-Kemper, B., Danabasoglu, G., Ferrari, R., Griffies, S., Hallberg, R., Holland, M., ... Samuels, B. (2011). Parameterization of mixed layer eddies. iii: Implementation and impact in global ocean climate simulations. *Ocean Modelling*, 39(1-2), 61–78.
- Fox-Kemper, B., Ferrari, R., & Hallberg, R. (2008). Parameterization of mixed layer eddies. part i: Theory and diagnosis. *Journal of Physical Oceanography*, 38(6), 1145–1165.
- Frankignoul, C., & Hasselmann, K. (1977). Stochastic climate models, part ii application to sea-surface temperature anomalies and thermocline variability. *Tellus*, 29(4), 289–305.
- Gallmeier, K. M., Prochaska, J. X., Cornillon, P., Menemenlis, D., & Kelm, M. (2023). An evaluation of the llc4320 global ocean simulation based on the submesoscale structure of modeled sea surface temperature fields. *Geoscientific Model Development Discussions*, 1–42.
- Guillaumin, A. P., & Zanna, L. (2021). Stochastic-deep learning parameterization of ocean momentum forcing. *Journal of Advances in Modeling Earth Systems*, 13(9), e2021MS002534.
- Gula, J., Taylor, J., Shcherbina, A., & Mahadevan, A. (2022). Submesoscale processes and mixing. In *Ocean mixing* (pp. 181–214). Elsevier.
- Gultekin, C., Subel, A., Zhang, C., Leibovich, M., Perezhogin, P., Adcroft, A., ... Zanna, L. (2024). An analysis of deep learning parameterizations for ocean subgrid eddy forcing. *arXiv preprint arXiv:2411.06604*.
- Hoskins, B. J., & Bretherton, F. P. (1972). Atmospheric frontogenesis models: Mathematical formulation and solution. *Journal of the atmospheric sciences*, 29(1), 11–37.
- IPCC. (2019). *Special report on the ocean and cryosphere in a changing climate* [Book]. Cambridge, United Kingdom and New York, NY, USA: Cambridge University Press. doi: 10.1017/9781009157964
- IPCC. (2021). *Climate change 2021: The physical science basis. contribution of working group i to the sixth assessment report of the intergovernmental panel on climate change* (Vol. In Press) [Book]. Cambridge, United Kingdom and New York, NY, USA: Cambridge University Press. doi: 10.1017/9781009157896
- Johnson, L., Lee, C. M., & D’Asaro, E. A. (2016). Global estimates of lateral spring-time restratification. *Journal of Physical Oceanography*, 46(5), 1555–1573.
- Lapeyre, G., Klein, P., & Hua, B. L. (2006). Oceanic restratification forced by surface frontogenesis. *Journal of Physical Oceanography*, 36(8), 1577–1590.
- Large, W. G., McWilliams, J. C., & Doney, S. C. (1994). Oceanic vertical mixing: A review and a model with a nonlocal boundary layer parameterization. *Reviews of geophysics*, 32(4), 363–403.
- Mahadevan, A., Tandon, A., & Ferrari, R. (2010). Rapid changes in mixed layer stratification driven by submesoscale instabilities and winds. *Journal of Geophysical Research: Oceans*, 115(C3).
- McWilliams, J. C. (2016). Submesoscale currents in the ocean. *Proceedings of the Royal Society A: Mathematical, Physical and Engineering Sciences*, 472(2189), 20160117.
- Menemenlis, D., Campin, J.-M., Heimbach, P., Hill, C., Lee, T., Nguyen, A., ... Zhang, H. (2008). Ecco2: High resolution global ocean and sea ice data synthesis. *Mercator Ocean Quarterly Newsletter*, 31(October), 13–21.
- Menemenlis, D., Hill, C., Henze, C., Wang, J., & Fenty, I. (2021). *Pre-swot level-4 hourly mitgcm llc4320 native 2km grid oceanographic version 1.0*. Ver.
- Morrow, R., Fu, L.-L., Arduin, F., Benkiran, M., Chapron, B., Cosme, E., ... others (2019). Global observations of fine-scale ocean surface topography with

- the surface water and ocean topography (swot) mission. *Frontiers in Marine Science*, 6, 232.
- Otness, K., Zanna, L., & Bruna, J. (2023). Data-driven multiscale modeling of sub-grid parameterizations in climate models. *arXiv preprint arXiv:2303.17496*.
- Perezhogin, P., Zanna, L., & Fernandez-Granda, C. (2023). Generative data-driven approaches for stochastic subgrid parameterizations in an idealized ocean model. *arXiv preprint arXiv:2302.07984*.
- Qiu, B., Chen, S., Klein, P., Ubelmann, C., Fu, L.-L., & Sasaki, H. (2016). Reconstructability of three-dimensional upper-ocean circulation from swot sea surface height measurements. *Journal of Physical Oceanography*, 46(3), 947–963.
- Reichl, B. G., & Hallberg, R. (2018). A simplified energetics based planetary boundary layer (epbl) approach for ocean climate simulations. *Ocean Modelling*, 132, 112–129.
- Ribeiro, M. T., Singh, S., & Guestrin, C. (2016). ” why should i trust you?” explaining the predictions of any classifier. In *Proceedings of the 22nd acm sigkdd international conference on knowledge discovery and data mining* (pp. 1135–1144).
- Rocha, C. B., Chereskin, T. K., Gille, S. T., & Menemenlis, D. (2016). Mesoscale to submesoscale wavenumber spectra in drake passage. *Journal of Physical Oceanography*, 46(2), 601–620.
- Ross, A., Li, Z., Perezhogin, P., Fernandez-Granda, C., & Zanna, L. (2023). Benchmarking of machine learning ocean subgrid parameterizations in an idealized model. *Journal of Advances in Modeling Earth Systems*, 15(1), e2022MS003258.
- Sagaut, P. (2005). *Large eddy simulation for incompressible flows: an introduction*. Springer Science & Business Media.
- Sane, A., Reichl, B. G., Adcroft, A., & Zanna, L. (2023). Parameterizing vertical mixing coefficients in the ocean surface boundary layer using neural networks. *arXiv preprint arXiv:2306.09045*.
- Selvaraju, R. R., Cogswell, M., Das, A., Vedantam, R., Parikh, D., & Batra, D. (2017). Grad-cam: Visual explanations from deep networks via gradient-based localization. In *Proceedings of the ieee international conference on computer vision* (pp. 618–626).
- Shakespeare, C. J., & Taylor, J. R. (2013). A generalized mathematical model of geostrophic adjustment and frontogenesis: uniform potential vorticity. *Journal of fluid mechanics*, 736, 366–413.
- Shamekh, S., Lamb, K. D., Huang, Y., & Gentine, P. (2023). Implicit learning of convective organization explains precipitation stochasticity. *Proceedings of the National Academy of Sciences*, 120(20), e2216158120.
- Shcherbina, A. Y., D’Asaro, E. A., Lee, C. M., Klymak, J. M., Molemaker, M. J., & McWilliams, J. C. (2013). Statistics of vertical vorticity, divergence, and strain in a developed submesoscale turbulence field. *Geophysical Research Letters*, 40(17), 4706–4711.
- Sinha, A., Callies, J., & Menemenlis, D. (2023). Do submesoscales affect the large-scale structure of the upper ocean? *Journal of Physical Oceanography*, 53(4), 1025–1040.
- Souza, A. N., Wagner, G., Ramadhan, A., Allen, B., Churavy, V., Schloss, J., . . . others (2020). Uncertainty quantification of ocean parameterizations: Application to the k-profile-parameterization for penetrative convection. *Journal of Advances in Modeling Earth Systems*, 12(12), e2020MS002108.
- Su, Z., Torres, H., Klein, P., Thompson, A. F., Siegelman, L., Wang, J., . . . Hill, C. (2020). High-frequency submesoscale motions enhance the upward vertical heat transport in the global ocean. *Journal of Geophysical Research: Oceans*, 125(9), e2020JC016544.

- Su, Z., Wang, J., Klein, P., Thompson, A. F., & Menemenlis, D. (2018). Ocean submesoscales as a key component of the global heat budget. *Nature communications*, 9(1), 775.
- Taylor, J. R., & Thompson, A. F. (2023). Submesoscale dynamics in the upper ocean. *Annual Review of Fluid Mechanics*, 55, 103–127.
- Torres, H. S., Klein, P., Menemenlis, D., Qiu, B., Su, Z., Wang, J., . . . Fu, L.-L. (2018). Partitioning ocean motions into balanced motions and internal gravity waves: A modeling study in anticipation of future space missions. *Journal of Geophysical Research: Oceans*, 123(11), 8084–8105.
- Treguier, A.-M., de Boyer Montégut, C., Bozec, A., Chassignet, E. P., Fox-Kemper, B., Hogg, A. M., . . . others (2023). The mixed layer depth in the ocean model intercomparison project (omip): Impact of resolving mesoscale eddies. *EGUsphere*.
- Uchida, T., Balwada, D., Abernathey, R., McKinley, G., Smith, S., & Levy, M. (2019). The contribution of submesoscale over mesoscale eddy iron transport in the open southern ocean. *Journal of Advances in Modeling Earth Systems*, 11(12), 3934–3958.
- Uchida, T., Le Sommer, J., Stern, C., Abernathey, R., Holdgraf, C., Albert, A., . . . others (2022). Cloud-based framework for inter-comparing submesoscale permitting realistic ocean models. *Geoscientific Model Development Discussions*, 1–32.
- Van den Broeck, G., Lykov, A., Schleich, M., & Suci, D. (2022). On the tractability of shap explanations. *Journal of Artificial Intelligence Research*, 74, 851–886.
- Wang, P., Yuval, J., & O’Gorman, P. A. (2022). Non-local parameterization of atmospheric subgrid processes with neural networks. *Journal of Advances in Modeling Earth Systems*, 14(10), e2022MS002984.
- Xiao, Q., Balwada, D., Jones, C. S., Herrero-González, M., Smith, K. S., & Abernathey, R. (2023). Reconstruction of surface kinematics from sea surface height using neural networks. *Journal of Advances in Modeling Earth Systems*, 15(10), e2023MS003709.
- Yuval, J., & O’Gorman, P. A. (2020). Stable machine-learning parameterization of subgrid processes for climate modeling at a range of resolutions. *Nature communications*, 11(1), 3295.
- Zanna, L., & Bolton, T. (2020). Data-driven equation discovery of ocean mesoscale closures. *Geophysical Research Letters*, 47(17), e2020GL088376.
- Zeiler, M. D., & Fergus, R. (2014). Visualizing and understanding convolutional networks. In *Computer vision—eccv 2014: 13th european conference, zurich, switzerland, september 6–12, 2014, proceedings, part i 13* (pp. 818–833).
- Zhang, C., Perezhugin, P., Gultekin, C., Adcroft, A., Fernandez-Granda, C., & Zanna, L. (2023). Implementation and evaluation of a machine learned mesoscale eddy parameterization into a numerical ocean circulation model. *arXiv preprint arXiv:2303.00962*.
- Zhang, J., Zhang, Z., & Qiu, B. (2023). Parameterizing submesoscale vertical buoyancy flux by simultaneously considering baroclinic instability and strain-induced frontogenesis. *Geophysical Research Letters*, 50(8), e2022GL102292.
- Zhou, S., Dong, J., Xu, F., Jing, Z., & Dong, C. (2024). A neural network-based submesoscale vertical heat flux parameterization and its implementation in regional ocean modeling system (roms). *arXiv preprint arXiv:2403.05028*.
- Zhu, R., Li, Y., Chen, Z., Du, T., Zhang, Y., Li, Z., . . . Wu, L. (2023). Deep learning improves reconstruction of ocean vertical velocity. *Geophysical Research Letters*, 50(19), e2023GL104889.

S1 Calculation of R^2 values

The R^2 metric is computed by,

$$R^2 = 1 - \frac{\sum_i (\mathbb{Y}_{wb,i} - \hat{\mathbb{Y}}_{wb,i})^2}{\sum_i (\mathbb{Y}_{wb,i} - \langle \mathbb{Y}_{wb} \rangle)^2}, \quad (\text{S1})$$

where $\mathbb{Y}_{wb,i}$ is the target subgrid flux (at location i) as defined in Table 1, $\hat{\mathbb{Y}}_{wb,i}$ is the same for prediction of \mathbb{Y}_{wb} by the CNN or MLE parameterization, and $\langle \mathbb{Y}_{wb} \rangle = \frac{1}{n} \sum_{i=1}^n \mathbb{Y}_{wb,i}$ is the mean of \mathbb{Y}_{wb} over all n samples.

S2 The MLE parameterization

The MLE parameterization is cast in the form of a streamfunction Ψ_{MLE} (Fox-Kemper et al., 2008), provided by a scaling for,

$$\overline{w'b'}^z \propto \frac{H_{ML} |\overline{\nabla_H b}|^z}{|f|}, \quad (\text{S2})$$

where H_{ML} is the mixed layer depth, f is the Coriolis parameter, w is vertical velocity, b is buoyancy, and $\nabla_H b$ is the horizontal buoyancy gradient. We follow the notation in Fox-Kemper et al. (2008), where the horizontal spatial resolution of the GCM is denoted (\cdot) and $(\cdot)'$ is the unresolved subgrid variable. Superscript z represents a vertical average over the mixed layer depth. The scaling for submesoscale vertical buoyancy flux, $\overline{w'b'}^z$, is derived from the bulk extraction of potential energy by mixed layer eddies. A shape function $\mu(z)$ estimates the depth, z , at which the mixed layer eddy fluxes are activated,

$$\mu(z) = \max \left(0, \left[1 - \left(\frac{2z}{H_{ML}} + 1 \right)^2 \right] \left[1 + \frac{5}{21} \left(\frac{2z}{H_{ML}} + 1 \right)^2 \right] \right), \quad (\text{S3})$$

where $\mu(z)$ is set to vanish at the surface and below the mixed layer H_{ML} .

Region	Latitudinal Range	Longitudinal Range
1. California Current	(30,45)	(-140,-125)
2. Gulf Stream	(30,45)	(-60,-45)
3. Kuroshio Extension	(25,40)	(145,160)
4. North Pacific	(10,25)	(-180,-165)
5. Arabian Sea	(0,15)	(55,70)
6. Equatorial Atlantic	(-8,8)	(-30,-15)
7. Indian Ocean	(-25,-10)	(70,85)
8. South Atlantic	(-30,-15)	(-25,-10)
9. South Pacific	(-45,-30)	(-140,-125)
10. Malvinas Current	(-55,-40)	(-60,-45)
11. Agulhas Current	(-55,-40)	(20,35)
12. Southern Ocean, New Zealand	(-60,-45)	(-175,-160)

Table S1. Coordinate range of sampled regions from the LLC4320 used in this study, corresponding to the blue boxes in Figure 1.

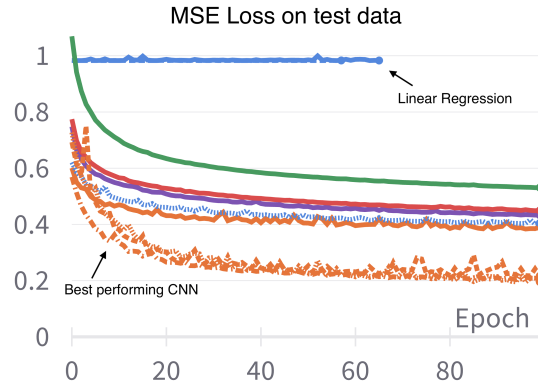


Figure S1. Example of the loss function during the hyper-parameter sweep of the CNN in the $1/4^\circ$ filter scale experiment. Solid blue line is the case of a simple linear regression, which is not sufficient to reduce the MSE loss.

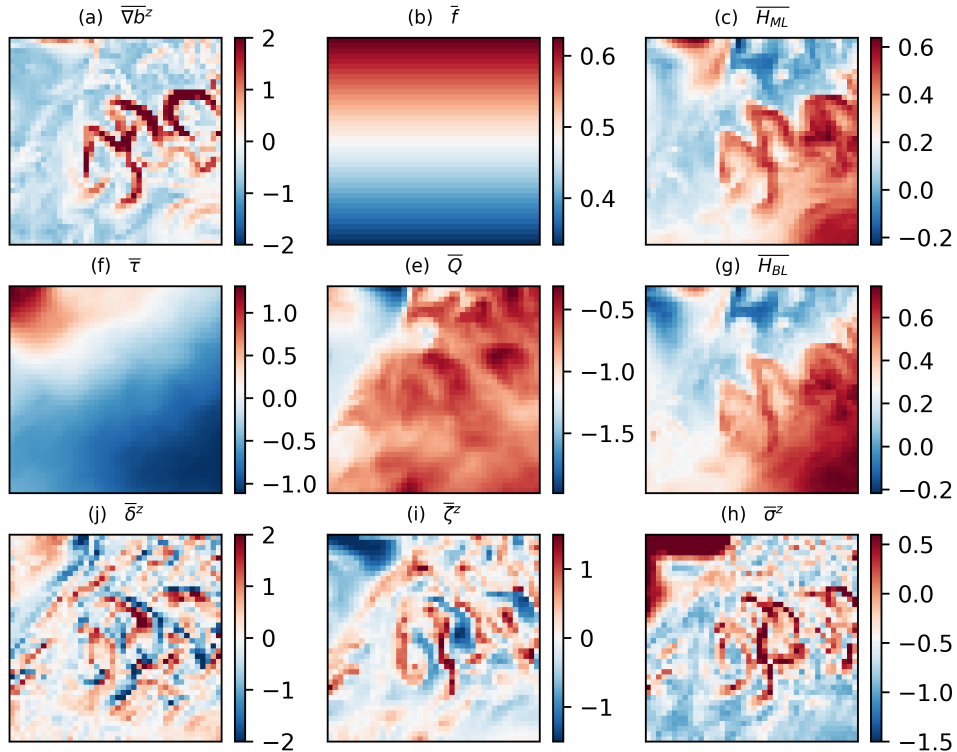


Figure S2. Snapshots of the normalized input features (corresponding to Table 1) in the $1/4^\circ$ filter scale.

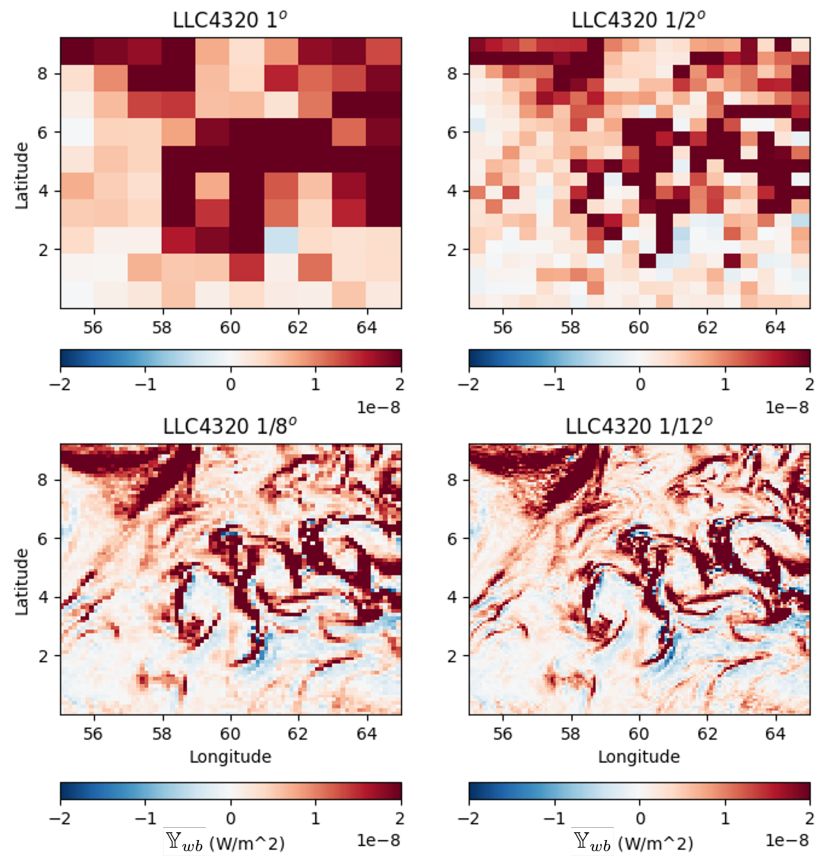


Figure S3. A snapshot as in Figure 4a to illustrate the CNN output Υ_{wb} (W/m²) with filter scales of 1°, 1/2°, 1/8°, 1/12°.

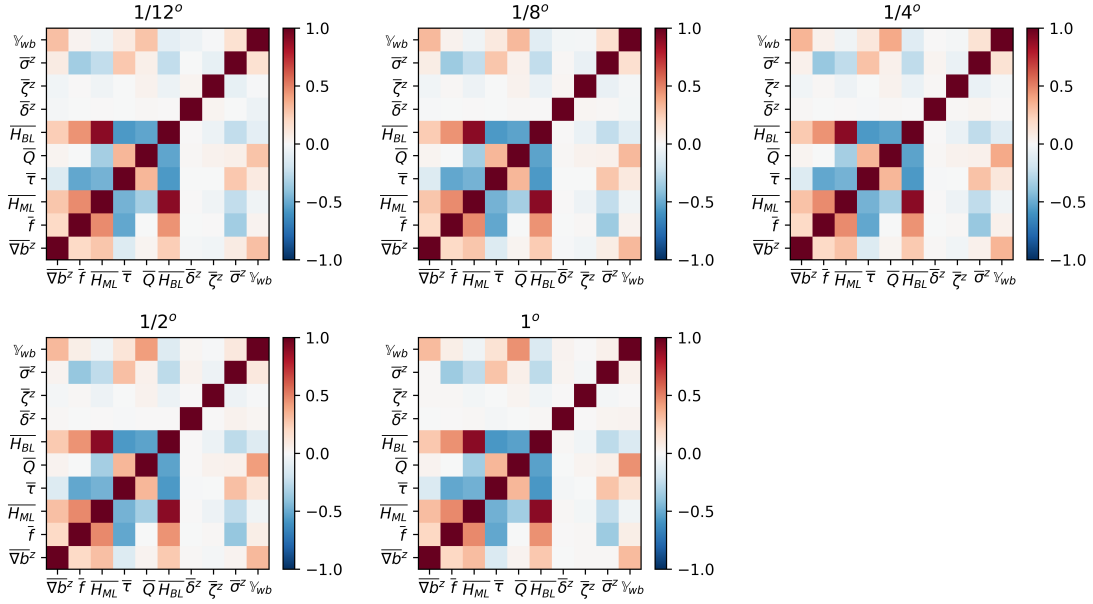


Figure S4. Correlation maps between all input features and output (corresponding to Table 1) over the entire dataset used for training and testing. Examples of each filter scale applied to data are shown for comparison: 1° , $1/2^\circ$, $1/4^\circ$, $1/8^\circ$, $1/12^\circ$. Variables associated with surface forcing (e.g., $\overline{H_{BL}}$, \overline{Q} , $\overline{\tau}$ demonstrate the largest correlation and anti-correlation with each other, dependent on the sign convention). The CNN output, \mathbb{Y}_{wb} shows no correlations above 0.2 with any of the input features.

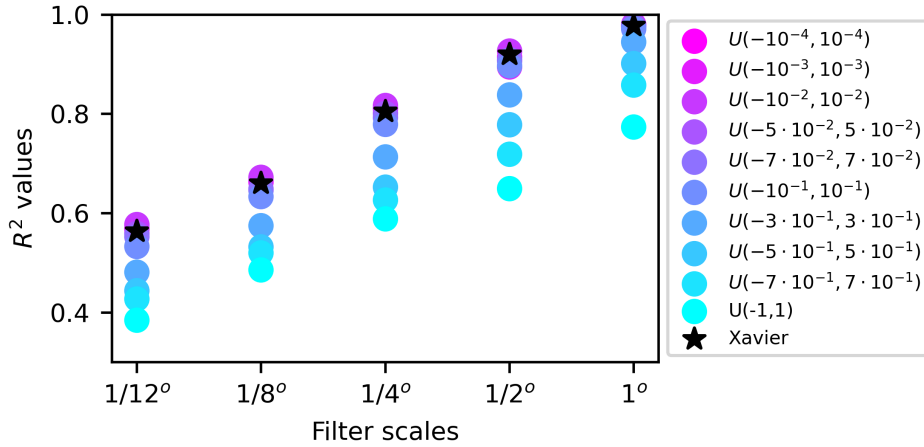


Figure S5. Uniform distributions for weight initializations (noted in the legend by the upper and lower bounds) against the default Xavier initialization in Pytorch, which is a function of the number of input channels. It is shown that the R^2 values computed over the entire unseen dataset is sensitive to the choice of weight initialization. However, the spread in R^2 from different initializations is small compared to the different sensitivity tests performed in the main text as long as the distribution bounds stay below 0.1.